Efficient Heat Dissipation of Photonic Crystal Microcavity by Monolayer Graphene

Min-Hsiung Shih,[†,∥,*] Lain-Jong Li,[‡,§] Yi-Chun Yang,[†] Hsiang-Yu Chou,[†] Cheng-Te Lin,[‡] and Ching-Yuan Su[‡,⊥]

[†]Research Center of Applied Sciences (RCAS), Academia Sinica, Taipei 11529, Taiwan, [‡]Institute of Atomic and Molecular Sciences, Academia Sinica, Taipei 10617, Taiwan, [§]Department of Medical Research, China Medical University Hospital, Taichung 40402 Taiwan, [⊥]Department of Electronic Engineering, Chang Gung University, Tao-Yuan 33302, Taiwan, and [∥]Department of Photonics, National Chiao Tung University, Hsinchu 30010, Taiwan

ABSTRACT Graphene, which exhibits excellent thermal conductivity, is a potential heat dissipation medium for compact optoelectronic devices. Photonic devices normally produce large- quantity of unwanted heat, and thus, a heat dissipation strategy is urgently needed. In this study, single-layer graphene (SLG) grown by chemical vapor deposition (CVD) is used to cover the surface of a photonic crystal (PhC) cavity, where the heat flux produced by the PhC cavity can be efficiently dissipated along the in-plane direction of the SLG. The thermal properties of the graphene-capped PhC cavity were characterized by experiments and theoretical calculations. The thermal resistance of the SLG-capped PhC cavity obtained from experiments is lower than half of that of a bare PhC cavity. The temperature of a SLG-capped PhC cavity is 45 K lower than that without SLG capping under an optical power of 100 μW. Our simulation results indicate that SLG receives the majority of the heat fluxes from the device, leading to the efficient heat dissipation. Both the experimental and simulation results suggest that the SLG is a promising material to enhance the heat dissipation efficiency for optoelectronic applications.

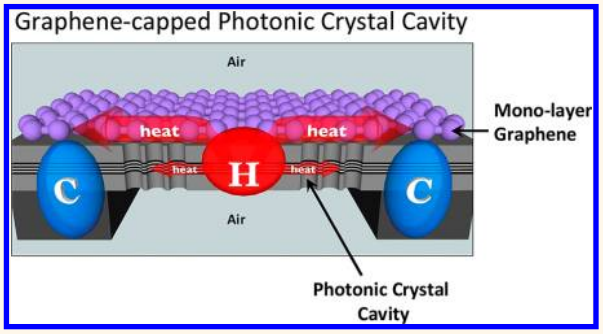

KEYWORDS: graphene · photonic crystals · heat dissipation · thermal resistance · optical cavity

Graphene is a two-dimensional (2D) material composed of carbon atoms arranged in a hexagonal lattice. This carbon monatomic layer and its excellent electrical and thermal properties, discovered by a research group at the University of Manchester in 2004,[1] have received great attention from scientists and engineers. In addition to the electrical properties and related devices,[2−6] its mechanical,[7−9] optical,[10−14] photovoltaic applications[15,16] and thermal properties[17−21] have been widely studied. Most of the properties of graphene are dominated by the highly anisotropic nature of graphene crystals. In the in-plane direction, carbon atoms are bonded with each other through covalent sp^2 bonds, which are among the strongest bonds in natural materials. However, the interaction between each graphene layer, or with the overlying and underlying materials, is through weak van der Waals forces. This results in the asymmetric and unusual properties of graphene, including its thermal conductivity. The thermal conductivity values of the suspended and supported single-layer graphenes (SLGs) are distinctly different. For the suspended SLGs, values of 3000−5000 W/m·K have been reported in both theoretical prediction[22−26] and experiments.[17,18,27,28] By contrast, the thermal conductivity of supported SLG is approximately 600 W/m·K;[29,30] however, it is still substantially higher than that of copper, gold, and silver, which are used as heat dissipating material in optoelectronic devices. Owing to the excellent thermal conductivity of graphene, multilayered graphene has been demonstrated as heat dissipation medium in the SOI and GaN transistors for integrated circuits.[31,32]

In the past few decades, 2D photonic crystal (PhC) cavities have become a promising technology for creating compact and efficient light sources[33−37] in dense chip-scale optical systems. Most photonic crystal cavities are implanted in suspended membrane structures (air-dielectric-air) to achieve improved vertical optical confinement in the

* Address correspondence to mhshih@gate.sinica.edu.tw.

Received for review August 6, 2013 and accepted November 11, 2013.

Published online November 11, 2013
10.1021/nn404097s

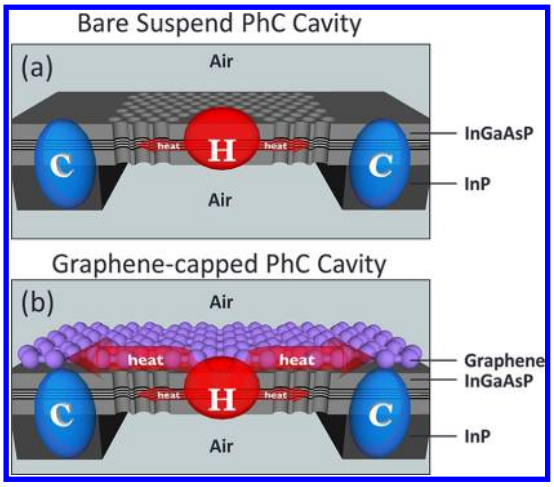

Figure 1. Illustration of heat flux dissipation in a suspended-membrane PhC microcavity (a) without SLG and (b) with SLG. (a) In a bare suspended PhC cavity, the thermal flux propagate mainly through the InGaAsP layer because the thermal conductivity of air is much lower than that of InGaAsP. (b) In a graphene-capped PhC cavity, the majority of the heat flux passes through the SLG, and the remaining heat passes through the gain material InGaAsP layer.

minute cavity, which is illustrated in Figure 1a. However, thermal accumulation is a critical problem when optical energy is localized within a submicrometer region. A superabundance of heat raises the temperature and the probability of nonradiative recombination, leading to suppressed emission efficiencies. Furthermore, because of the poor thermal conductivity of air, the high temperature caused by the heat accumulation within thin membranes likely damages the devices. Several reports have adopted the substances with high thermal conductivity such as such as SOI,[38] sapphire,[39] and MgF2-diamond[40] to dissipate the heat in compact PhC laser devices. However, the added-on substrates can reduce index contrast and degrade optical confinement in the vertical direction because of the higher index of the substrate,[32] which results in a high lasing threshold and a poor emission performance for the compact PhC emitters. Therefore, a thin SLG possessing high thermal conductivity is an excellent candidate material for solving the heat accumulation issue in compact PhC cavities.

In this study, a SLG is integrated with a compact PhC microcavity. The optical intensity of a PhC cavity is highly confined around the center of the cavity, and the thermal energy dissipates through the air-bridge membrane to the substrate as shown in Figure 1a. When SLG is placed on the top of the PhC cavity as shown in Figure 1b, the thermal flux is parallel to the lateral direction of the SLG, which is the most efficient thermal dissipation direction of the SLG. Because the SLG is ultrathin and exhibits extremely high thermal conductivity, a SLG-capped PhC microcavity not only maintains good optical confinement but also and exhibits considerably better thermal properties than a bare cavity. Furthermore, SLG that exhibits high electron mobility is a potential contact in the electrically pumped scheme used in compact PhC emitters.

TABLE 1. Parameters of Materials Used in Heat Transfer Simulation

material	air	InGaAsP	graphene
Density ρ (kg/m^3)	1.1758	5088.4	2200[a]
Thermal conductivity k (W/m·K)	0.0262	4.2[b]	4000 (suspended) 600 (supported)
Specific heat capacity C_p (J/kg·K)	1015.415	334.8	1959

[a] Reference 41−43. [b] Reference 44.

RESULTS AND DISCUSSION

Simulation. Before fabricating the SLG-capped PhC microcavity, a three-dimensional (3D) finite-element method (FEM) was used to examine the thermal properties of the proposed system. The air-bridge-type D3 PhC microcavity used in this study contains a 240-nm-thick InGaAsP layer and a 2-μm defect size to confine the optical intensity within the cavity. The single-layer graphene with a thickness of 0.3 nm was placed on the top of PhC cavity. The thickness of air layers were set to be 5 μm on the top and bottom of the SLG/PhC cavity. A circular 100-μW heat source was placed in the center of the cavity. All simulations were performed during continuous-wave (CW) injection at room temperature (300 K). The parameters of the various materials used in the simulation are listed in Table 1.

The reported thermal conductivity values for SLG vary probably due to different estimation methods and experimental conditions. In our simulations, we used the values 4000 W/m·K for suspended SLG[28] and 600 W/m·K for supported SLG.[29,30] Since the strong length dependence of the grapheme thermal conductivity,[45−48] the thermal conductivities of the suspended and supported SLGs were applied for the air-hole area and substrate area in the simulation. An effective thermal conductivity k_{eff} of SLG was them used in the graphene-capped PhC microcavity system. For the simulated PhC microcavity, the distance between air holes was 500 nm and the radius of the air holes was 150 nm. Therefore, the ratio of suspended to supported SLG ranged between 28.26% and 71.76%, and they were assumed to be series wound. SLG exhibited a $k_{eff} = 4000 \times 28.26\% + 600 \times 71.76\% = 1560.96$ W/m·K. More accurate thermal transportation behavior in the SLG/PhC device could be obtained by including the interface thermal resistance between SLG and PhC[49−51] in the simulation. The 3D FEM simulation results are shown in Figure 2. Figure 2a−c show the temperature distribution during the optical pumping with an optical power of 100 μW at the center of a 3-μm-diameter region for the InGaAsP bulk, the bare PhC microcavity, and the SLG-capped PhC microcavity,

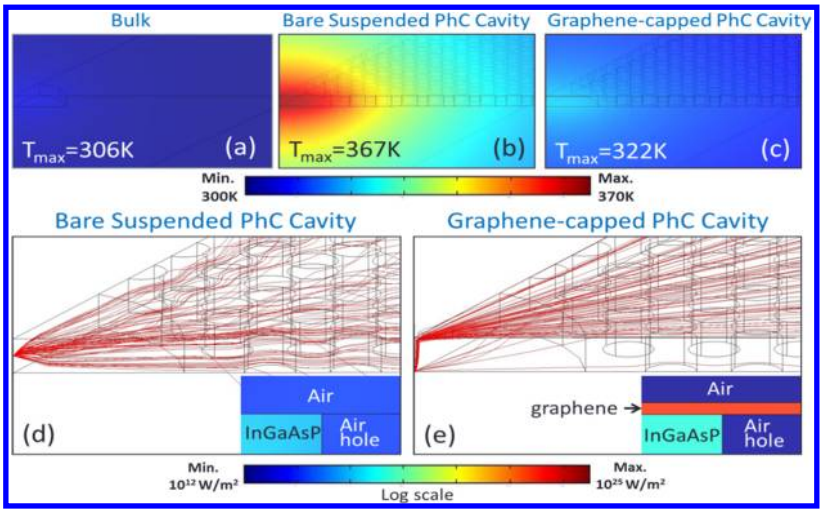

Figure 2. Simulated temperature distributions and heat flux using 3D FEM simulation under CW pumping conditions at an injected power of 0.1 mW and room temperature (300 K). In (a)–(c), the color scale represents temperature. (a) The maximal temperature for the bulk of material was 306 K, which is not much higher than room temperature. (b) The maximal temperature at the center of the suspended PhC cavity was 367 K. (c) The temperature at the center of the graphene-capped PhC cavity was 322 K, which is much lower than that in the bare PhC cavity at the same injected power. In (d) and (e), the red curves indicate simulated thermal fluxes. (d) All heat fluxes pass through the InGaAsP layer and are blocked by air holes. (e) Most heat fluxes penetrate the SLG layer and disperse directly. The color scale of the inserted figures in (d) and (e) shows the density of heat fluxes at the edge of an air hole. The thermal density is significantly higher in the SLG than in InGaAsP and air regions.

respectively, where the false colors represent different scales of the simulated temperature. The temperature in the bulk material rises only 6 K above 300 K (Figure 2a) because most of the heat can be dissipated through the substrate. However, the maximal temperature near the center of a suspended-membrane PhC microcavity under the same pumping condition is as high as 367 K (Figure 2b) because of the poor thermal conductivity of air. The significant temperature increase from 2(a) to 2(b) urges the application of an additional heat transport layer. Figure 2c shows that the temperature at the center of the graphene-capped PhC cavity is 322 K, which is markedly 45 K lower than that observed in a bare PhC cavity. Figure 2d,e show the details of how the simulated heat flux was transported in a bare suspended PhC cavity and a graphene-capped PhC cavity, respectively. Thermal energy is transported from the center of a cavity, a higher temperature site, to the edge of the cavity with a lower temperature. Figure 2d shows that heat fluxes pass through the slab and are blocked by the air holes. Figure 2e shows that the heat fluxes in the SLG propagate and disperse directly to the low temperature region. The insets in Figure 2d,e show the densities of the heat fluxes at the edges of the air holes in the two systems. The heat flux density in the InGaAsP and the air region is similar to each other, but is considerably higher in SLG. Thus, the dissipation of the heat flux in the PhC microcavity evidently benefits from the SLG.

Photonic Crystal Cavity Structures and Fabrication. PhC microcavities were fabricated in a 240-nm-thick InGaAsP layer that contained four InGaAsP-strained quantum wells (QWs) designed to emit nearly 1.55 μm

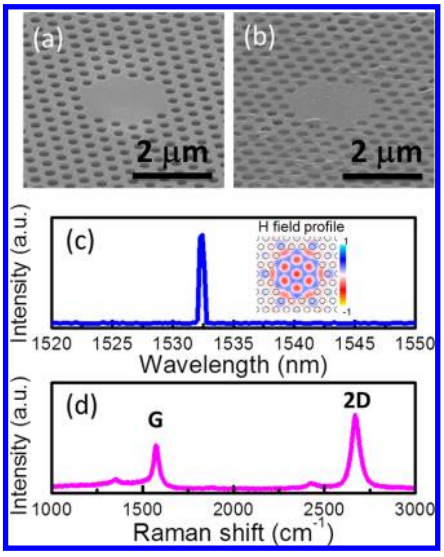

Figure 3. SEM images of the PhC microcavity (a) without SLG and (b) with SLG; (c) PL spectrum of the PhC microcavity with an emitted wavelength of approximately 1.55 μm. The inserted figure shows a 3D FDTD simulated magnetic field profile of the operating mode. It exhibits hexagonal, symmetrical behavior and fills the cavity. (d) Raman spectrum obtained from the graphene-capped cavity. The 2D peak is higher than the G peak, indicating the inclusion of SLG.

at room temperature. InGaAsP layers were deposited using metal–organic chemical vapor deposition (MOCVD) on an InP substrate. A silicon nitride (SiNx) layer was deposited using a plasma-enhanced chemical vapor deposition (PECVD) system, and a 5% polymethylmethacrylate (PMMA) resist was spin-coated onto the SiNx layer. Both SiNx and PMMA layers served as masks during subsequent fabrication processes.

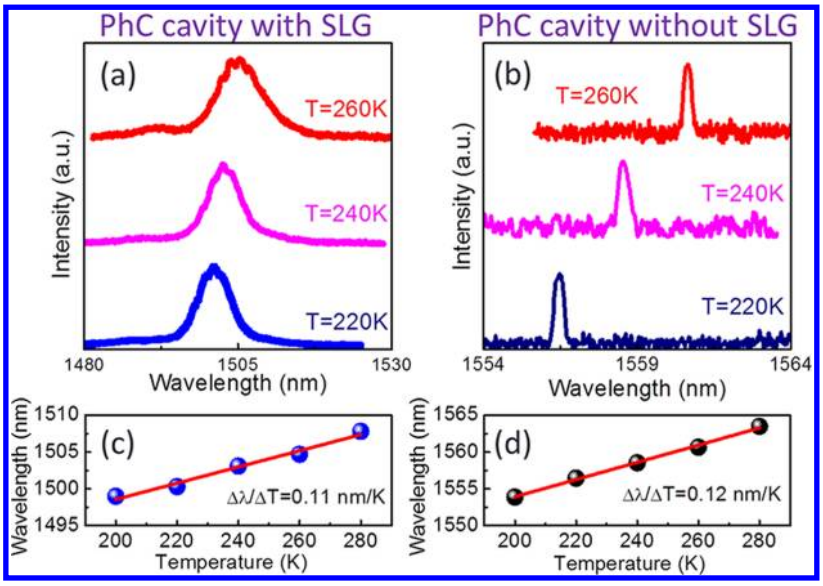

Figure 4. Temperature dependence of emission wavelengths in PhC microcavities with and without SLG under pulsed pumping conditions at a duty cycle of 1.5%: (a and b) Resonant spectra at 220, 240, and 260 K under a pumping of 0.5 mW; (c and d) emission wavelength from PhC cavities at different temperatures. The temperature dependence of emission wavelength in these two systems are 0.11 and 0.12 nm/K, respectively.

The PhC patterns were defined by using electron beam lithography and transferred into the SiNx mask and the InGaAsP layer by using an inductively coupled plasma (ICP) system with CHF_3/O_2 and $CH_4/Cl_2/H_2$ mixtures sequentially. All masks were removed at the end of the fabrication process. Suspended membranes were formed using an HCl solution during wet chemical etching at 0 °C. Figure 3a shows an SEM image of a suspended PhC microcavity. The defect region of the PhC cavity was approximately 2.0 μm in diameter. For the SLG-capped PhC cavity, a layer of CVD graphene was transferred onto the device substrate with cavities on it, where Figure 3b shows the SEM image of an SLG-capped PhC microcavity.

All devices were optically pumped using an 850-nm diode laser. The pump beam was focused on the devices using a 100× objective lens, and the spot size of the focused beam was approximately 2 μm in diameter. The output power emitted from the devices was collected using a multimode fiber connected to an optical spectrum analyzer. Figure 3c shows the photoluminescence (PL) spectrum of a bare PhC microcavity. On the basis of a 3D, finite-difference time-domain (FDTD) simulation, the operating mode was characterized as hexagonal, as shown in the inset in Figure 3c. To evaluate the quality of the SLG that was transferred, we used Raman spectroscopy; the Raman spectrum obtained using an excitation wavelength of 473 nm is shown in Figure 3d. There were two characteristic peaks: the G peak, which arises from stretching the C−C bond in graphitic materials and is common in all sp^2 carbon systems; and the 2D peak, which is the second order of zone-boundary photons. The 2D peak near 2700 cm^{-1} was higher than the G peak near 1580 cm^{-1}, indicating that high-quality SLG, rather than graphite, was placed on the microcavity.[52]

Measurements of Thermal Properties. A critical parameter for the thermal property of the devices is thermal resistance R_{th}, which is defined as the rate of temperature variation in devices caused by absorbing the pumped power. Thermal resistance is described as the following formula:

$$R_{th} = \frac{\Delta T}{\Delta P} \quad (1)$$

where ΔT and ΔP are the changes in temperature and incident power, respectively. To evaluate the thermal resistance of PhC microcavities, we measure emission wavelengths at various environmental temperatures and pumping powers. Thermal resistance was then calculated directly by

$$R_{th} = \frac{\Delta T}{\Delta P} = \frac{\Delta\lambda/\Delta P}{\Delta\lambda/\Delta T} \quad (2)$$

To characterize the emission wavelength at various temperatures, the devices were placed in a cryostat under the pressure of 5.0×10^{-6} mTorr and the same pumping conditions. Figure 4a,b shows the spectra of SLG-capped and bare microcavities, respectively, at 220, 240, and 260 K under a pumping of 0.5 mW. When the temperature is increased, the wavelength of the resonant peaks increases in both systems. Moreover, we record the resonant peaks when the surrounding temperature is changed from 200 to 280 K at 20 K intervals, and the results are shown in Figure 4c,d. The resonant wavelength of the graphene-capped microcavity red-shifts with a rate of $\Delta\lambda/\Delta T \approx 0.11$ nm/K (Figure 4c), which is similar to

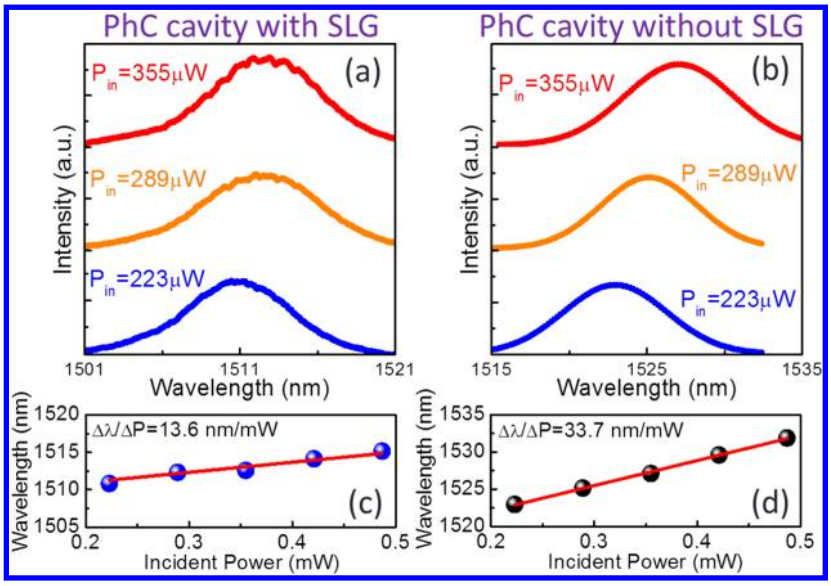

Figure 5. Power dependence of resonant wavelengths in PhC microcavities with and without SLG under CW pumping conditions at an environmental temperature of 200 K: (a and b) resonant spectra at injected powers of 223, 289, and 355 μW, respectively; (c and d) wavelength shifting within 0.2−0.5 mW. The power dependence of a bare PhC microcavity is 33.7 nm/mW, but that of a PhC microcavity with SLG is only 13.6 nm/mW. The heat dissipation is evidently much more efficient in the graphene-capped PhC microcavity.

the rate for the bare microcavity ($\Delta\lambda/\Delta T \approx 0.12$ nm/K) (Figure 4d).

Next, we measured the power-dependent wavelength shifts under CW operation conditions at 200 K and the results are presented in Figure 5. Figure 5a,b shows the resonant spectra of SLG-capped and bare microcavities pumped with three powers, 223, 289, and 355 μW. In both PhC microcavities, the resonant peaks red-shift when the pumping power is increased. We collected the red-shift data of the resonant peaks when the pumping power is increased from 0.2 to 0.5 mW, and the results are shown in Figures 5c,d. Unlike insensitive wavelength shift on temperature, the disparity in the power dependence of wavelength for the two systems, the SLG-capped and bare PhC microcavities, is large. For the SLG-capped microcavity, $\Delta\lambda/\Delta P$ is approximately 13.6 nm/mW (Figure 5c), whereas the $\Delta\lambda/\Delta P$ is up to 33.7 nm/mW for the bare microcavity. The variation of the emission wavelength and line width between PhC cavities with and without SLG is attributed to the SLG roughness on the PhC cavity.

By substituting the experimental values of $\Delta\lambda/\Delta T$ and $\Delta\lambda/\Delta P$ into eq 2, we obtain the experimental thermal resistances of the two systems: for the graphene-capped microcavity, $R_{th} \approx 124$ K/mW, and for the bare microcavity, $R_{th} \approx 281$ K/mW. Thus, the thermal conductivity of the SLG-capped PhC cavity is more than two times larger than the value measured for the bare PhC cavity, indicating that the high thermal conductivity of SLG helps dissipate the heat generated around the center of cavity. In simulation, we also observed the SLG-capped PhC cavity exhibits more than two times larger thermal conductivity than the bare PhC cavity (thermal resistance SLG/PhC, 218 K/mW; bare PhC, 574 K/mW). The thermal properties and parameters of SLG-capped and bare PhC cavities are listed in Table 2.

TABLE 2. Experimental Results and Estimated Thermal Resistance

parameters	PhC cavity with SLG	PhC cavity without SLG
$\Delta\lambda/\Delta T$(nm/K)	0.11	0.12
$\Delta\lambda/\Delta P$(nm/mK)	13.6	33.7
R_{th} (K/mW)	124	281

In the experiment, the temperature-dependent wavelength shifts and the $\Delta\lambda/\Delta T$ values in two PhC cavities are similar. In contrast, the power-dependent wavelength shifts of the two systems significantly vary, which implies that the heat dissipation determines the temperature increase in minute regions under CW operation. SLG, which has excellent thermal conductivity, helps to spread the heat effectively in the graphene-capped PhC microcavity, and the thermal resistance of the graphene-capped microcavity is less than half of that of the bare microcavity. Thus, the experimental and simulated results both demonstrate that the thin SLG substantially improves heat dissipation in the compact PhC cavity. We should note the temperature dependence of thermal conductance of the SLG had been reported.[29] We expected a small variation in thermal resistance of the whole device when temperature is increased from 200 K to room temperature.

CONCLUSION

In this study, we develop a SLG-capped PhC microcavity. The thermal properties of the PhC microcavities with and without graphene-capping are characterized

theoretically and experimentally. The results of 3D FEM simulations show that the SLG receives the bulk of the heat fluxes during the dissipative process, leading to the lower temperature at the center of the graphene-capped PhC cavity. Experimental results demonstrate that the thermal resistance of the bare PhC microcavity is approximately 281 K/mW, but that of the graphene-capped PhC microcavity is only 124 K/mW. The results of our simulations and experiments consistently demonstrate that SLG facilitates the heat dissipation in the PhC microcavity. The SLG is a promising material to enhance the heat dissipation efficiency for optoelectronic applications.

METHODS

CVD Growth of Graphene. Large-area graphene films were synthesized on copper foil (Alfa Aesar, purity 99.8% ; 25 μm thick) by chemical vapor deposition in a hot-wall tube furnace. A copper (Cu) foil was loaded into the center of the tube, and the system was flushed with a constant flow of hydrogen (415 sccm) at 760 mTorr for 50 min. The Cu foil was annealed at 1000 °C for 40 min to remove organic matter and oxides from the surface. A gas mixture of methane and hydrogen (CH_4 = 60 sccm and H_2 = 15 sccm at 750 mTorr) was introduced into the system at 1000 °C for graphene layer growth. After growth of the graphene films, the graphene/Cu foil was cooled to 25 °C to complete the growth.

Au-Assisted Transfer Process of Graphene. To transfer graphene from a Cu foil to a PhC cavity, a thin layer of Au (30 nm) was sputtered on graphene.[53] The Au/graphene/Cu stack film was immersed in an ammonium persulphate solution (Aldrich, 1 M) at 60 °C for 2 h to dissolve Cu foils. The Au-supported graphene was then thoroughly washed with deionized (DI) water. A target substrate with PhC cavities was used to fish the Au/graphene layers. After hot plate baking was performed at at 150 °C for 2 h, the PhC smaple with Au/graphene was immersed in a gold etching solution (Gold etchant type TFA from Transene Com.; content: iodine Complex, potassium iodide and water) for 10−20 min. Finally, the samples were rinsed with DI water to complete the transfer

Characterizations. Raman spectra were collected in a NT-MDT confocal Raman microscopic system (laser wavelength 473 nm and laser spot size ~0.5 μm). The Si peak at 520 cm^{-1} was used as reference for wavenumber calibration. The emission of the PhC cavity was characterized by a micro-PL system with a cryogenic system. The cavity was optically pumped at room temperature using an 850 nm diode laser at normal incidence. The pumped spot was focused by a 100× objective lens to a spot approximately 2 μm in diameter. The output power was collected from the top of the cavity by a multimode fiber which was connected to an optical spectrum analyzer.

Conflict of Interest: The authors declare no competing financial interest.

Acknowledgment. The research was supported by the Nano Science and Technology Program, Academia Sinica and the National Science Council Taiwan (NSC 102-2112-M-001-019-MY3). The authors are also grateful to the Center for Nano Science and Technology in National Chiao Tung University.

REFERENCES AND NOTES

1. Novoselov, K. S.; Geim, A. K.; Morozov, S. V.; Jiang, D.; Zhang, Y.; Dubonos, S. V.; Grigorieva, I. V.; Firsov, A. A. Electric Field Effect in Atomically Thin Carbon Films. *Science* **2004**, *306*, 666–669.
2. Bolotin, K. I.; Sikes, K. J.; Jiang, Z.; Klima, M.; Fudenberg, G.; Hone, J.; Kim, P.; Stormer, H. L. Ultrahigh Electron Mobility in Suspended Grapheme. *Solid State Commun.* **2008**, *146*, 351–355.
3. Castro Neto, H.; Guinea, F.; Peres, N. M. R.; Novoselov, K. S.; Geim, A. K. The Electronic Properties of Grapheme. *Rev. Mod. Phys.* **2009**, *81*, 109–162.
4. He, Q.; Sudibya, H. G.; Yin, Z.; Wu, S.; Li, H.; Boey, F.; Huang, W.; Chen, P.; Zhang, H. Centimeter-Long and Large-Scale Micropatterns of Reduced Graphene Oxide Films: Fabrication and Sensing Applications. *ACS Nano* **2010**, *4*, 3201–3208.
5. Hong, T. K.; Lee, D. W.; Choi, H. J.; Shin, H. S.; Kim, B. S. Transparent, Flexible Conducting Hybrid Multilayer Thin Films of Multiwalled Carbon Nanotubes with Graphene Nanosheets. *ACS Nano* **2010**, *4*, 3861–3868.
6. Zeng, M.; Feng, Y.; Liang, G. Graphene-Based Spin Calloritronics. *Nano Lett.* **2011**, *11*, 1369–1373.
7. Frank, I. W.; Tanenbaum, D. M.; van der Zande, A. M.; McEuen, P. L. Mechanical Properties of Suspended Graphene Sheets. *J. Vac. Sci. Technol., B* **2007**, *25*, 2558–2561.
8. Lee, C.; Wei, Z.; Kysar, J. W.; Hone, J. Measurement of the Elastic Properties and Intrinsic Strength of Monolayer Graphene. *Science* **2008**, *321*, 385–388.
9. Suk, J. W.; Piner, R. D.; An, J.; Ruoff, R. S. Mechanical Properties of Monolayer Graphene Oxide. *ACS Nano* **2010**, *4*, 6557–6564.
10. Nair, R. R.; Blake, P.; Grigorenko, A. N.; Novoselov, K. S.; Booth, T. J.; Stauber, T.; Peres, N. M. R.; Geim, A. K. Fine Structure Constant Defines Visual Transparency of Graphene. *Science* **2008**, *320*, 1308–1308.
11. Zhang, Y.; Tang, T. T.; Girit, C.; Hao, Z.; Martin, M. C.; Zettl, A.; Crommie, M. F.; Shen, Y. R.; Wang, F. Direct Observation of a Widely Tunable Bandgap in Bilayer Graphene. *Nature* **2009**, *459*, 820–823.
12. Bonaccorso, F.; Sun, Z.; Hasan, T.; Ferrari, A. C. Graphene Photonics and Optoelectronics. *Nat. Photonics* **2010**, *4*, 611–622.
13. Lee, J.; Novoselov, K. S.; Shin, H. S. Interaction between Metal and Graphene:Dependence on the Layer Number of Graphene. *ACS Nano* **2011**, *5*, 608–612.
14. Tang, L.; Ji, R.; Li, X.; Teng, K. S.; Lau, S. P. Size-Dependent Structural and Optical Characteristics of Glucose-Derived Graphene Quantum Dots. *Part. Part. Syst. Charact.* **2013**, *30*, 523–531.
15. Yin, Z.; Sun, S.; Salim, T.; Wu, S.; Huang, X.; He, Q.; Lam, Y. M.; Zhang, H. Organic Photovoltaic Devices Using Highly Flexible Reduced Graphene Oxide Films as Transparent Electrodes. *ACS Nano* **2010**, *4*, 5263–5268.
16. Liu, Z.; Li, J.; Sun, Z. H.; Tai, G.; Lau, S. P.; Yan, F. The Application of Highly Doped Single-Layer Graphene as the Top Electrodes of Semitransparent Organic Solar Cells. *ACS Nano* **2012**, *6*, 810–818.
17. Balandin, A. A.; Ghosh, S.; Bao, W.; Calizo, I.; Teweldebrhan, D.; Miao, F.; Lau, C. N. Superior Thermal Conductivity of Single-Layer Graphene. *Nano Lett.* **2008**, *8*, 902–907.
18. Ghosh, S.; Calizo, I.; Teweldebrhan, D.; Pokatilov, E. P.; Nika, D. L.; Balandin, A. A.; Bao, W.; Miao, F.; Lau, C. N. Extremely High Thermal Conductivity of Graphene: Prospects for Thermal Management Applications in Nanoelectronic Circuits. *Appl. Phys. Lett.* **2008**, *92*, 151911-1–151911-3.
19. Prasher, R. Graphene Spreads the Heat. *Science* **2010**, *328*, 185–186.
20. Balandin, A. A. Thermal Properties of Graphene and Nanostructured Carbon Materials. *Nat. Mater.* **2011**, *10*, 569–581.
21. Xiao, N.; Dong, X.; Song, L.; Liu, D.; Tay, Y. Y.; Wu, S.; Li, L. J.; Zhao, Y.; Yu, T.; Zhang, H.; *et al.* Enhanced Thermopower of Graphene Films with Oxygen Plasma Treatment. *ACS Nano* **2011**, *5*, 2749–2755.
22. Nika, D. L.; Pokatilov, E. P.; Askerov, A. S.; Balandin, A. A. Phonon Thermal Conduction in Graphene: Role of

Umklapp and Edge Roughness Scattering. *Phys. Rev. B* **2009**, *79*, 155413–155424.
23. Nika, D. L.; Ghosh, S.; Pokatilov, E. P.; Balandin, A. A. Lattice Thermal Conductivity of Graphene Flakes: Comparison with Bulk Graphite. *Appl. Phys. Lett.* **2009**, *94*, 203103-1–203103-3.
24. Hu, J.; Ruan, X.; Chen, Y. P. Thermal Conductivity and Thermal Rectification in Graphene Nanoribbons: A Molecular Dynamics Study. *Nano Lett.* **2009**, *9*, 2730–2736.
25. Cao, A. Molecular Dynamics Simulation Study on Heat Transport in Monolayer Graphene Sheet with Various Geometries. *J. Appl. Phys.* **2012**, *111*, 083528-1–083528-9.
26. Nika, D. L.; Askerov, A. S.; Balandin, A. A. Anomalous Size Dependence of the Thermal Conductivity of Graphene Ribbons. *Nano Lett.* **2012**, *12*, 3238–3244.
27. Jauregui, L. A.; Yue, Y.; Sidorov, A. N.; Hu, J.; Yu, Q.; Lopez, G.; Jalilian, R.; Benjamin, D. K.; Delk, D. A.; Wu, W.; Liu, Z.; Wang, X.; Jiang, Z.; Ruan, X.; Bao, J.; Pei, S. S.; Chen, Y. P. Thermal Transport in Graphene Nanostructures: Experiments and Simulations. *ECS Trans.* **2010**, *28* (5), 73–83.
28. Chen, S.; Wu, Q.; Mishra, C.; Kang, J.; Zhang, H.; Cho, K.; Cai, W.; Balandin, A. A.; Ruoff, R. S. Thermal Conductivity of Isotopically Modified Graphene. *Nat. Mater.* **2012**, *11*, 203–207.
29. Seol, J. H.; Jo, I.; Moore, A. L.; Lindsay, L.; Aitken, Z. H.; Pettes, M. T.; Li, X.; Yao, Z.; Huang, R.; Broido, D.; Mingo, N.; Ruoff, R. S.; Shi, L. Two-Dimensional Phonon Transport in Supported Graphene. *Science* **2010**, *328*, 213–216.
30. Chen, J.; Zhang, G.; Li, B. Substrate Coupling Suppresses Size Dependence of Thermal Conductivity in Supported Graphene. *Nanoscale* **2013**, *5*, 532–536.
31. Subrina, S.; Kotchetkov, D.; Balandin, A. A. Heat Removal in Silicon-on-Insulator Integrated Circuits with Graphene Lateral Heat Spreaders. *IEEE Electron Device Lett.* **2009**, *30*, 1281–1283.
32. Yan, Z.; Liu, G.; Khan, J. M.; Balandin, A. A. Graphene Quilts for Thermal Management of High-Power GaN Transistors. *Nat. Commun.* **2012**, *3*, 827-1–827-8.
33. Painter, O.; Lee, R. K.; Scherer, A.; Yariv, A.; O'Brien, J. D.; Dapkus, P. D.; Kim, I. Two-Dimensional Photonic Band-Gap Defect Mode Laser. *Science* **1999**, *284*, 1819–1821.
34. Ellis, B.; Mayer, M. A.; Shambat, G.; Sarmiento, T.; Harris, J.; Haller, E. E.; Vučkovic, J. Ultralow-Threshold Electrically Pumped Quantum-Dot Photonic-Crystal Nanocavity Laser. *Nat. Photonics* **2011**, *5*, 297–300.
35. Park, H. G.; Kim, S. H.; Kwon, S. H.; Ju, Y. G.; Yang, J. K.; Baek, J. H.; Kim, S. B.; Lee, Y. H. Electrically Driven Single-Cell Photonic Crystal Laser. *Science* **2004**, *305*, 1444–1447.
36. Song, B. S.; Noda, S.; Asano, T.; Akahane, Y. Ultra-High-Q Photonic Double-Heterostructure Nanocavity. *Nat. Mater.* **2005**, *4*, 207–210.
37. Shih, M. H.; Kuang, W.; Mock, A.; Bagheri, M.; Hwang, E. H.; O'Brien, J. D.; Dapkus, P. D. High-Quality-Factor Photonic Crystal Heterostructure Laser. *Appl. Phys. Lett.* **2006**, *89*, 101104-1–101104-3.
38. Shih, M. H.; Mock, A.; Bagheri, M.; Suh, N. K.; Farrell, S.; Choi, S. J.; O'Brien, J. D.; Dapkus, P. D. Photonic Crystal Lasers in InGaAsP on a SiO_2/Si Substrates and Its Thermal Impedance. *Opt. Express* **2007**, *15*, 227–232.
39. Shih, M. H.; Yang, Y. C.; Liu, Y. C.; Chang, Z. C.; Hsu, K. S.; Wu, M. C. Room Temperature Continuous Wave Operation and Characterization of Photonic Crystal Nanolaser on a Sapphire Substrate. *J. Phys. D: Appl. Phys.* **2009**, *42*, 105113–105117.
40. Kim, S.; Lee, J.; Jeon, H. Over 1 h Continuous-Wave Operation of Photonic Crystal Lasers. *Opt. Express* **2011**, *19*, 1–6.
41. Bunch, J. S.; van der Zande, A. M.; Verbridge, S. S.; Frank, I. W.; Tanenbaum, A. M.; Parpia, J. M.; Craighead, H. G.; McEuen, P. L. Electromechanical Resonators from Graphene Sheets. *Science* **2007**, *315*, 490–493.
42. Chen, C.; Rosenblatt, S.; Bolotin, K. I.; Kalb, W.; Kim, P.; Kymissis, I.; Stormer, H. L.; Heinz, T. F.; Hone, J. Performance of Monolayer Graphene Nanomechanical Resonators with Electrical Readout. *Nat. Nanotechnol.* **2009**, *4*, 861–867.
43. Xu, Y.; Yan, S.; Jin, Z.; Wang, Y. Quantum-Squeezing Effects of Strained Multilayer Graphene NEMS. *Nanoscale Res. Lett,* **2011**, *6*, 355-1–355-6.
44. Matsuo, S.; Shinya, A.; Kakitsuka, T.; Nozaki, K.; Segawa, T.; Sato, T.; Kawaguchi, Y.; Notomi, M. High-Speed Ultracompact Buried Heterostructure Photonic-Crystal Laser with 13 fJ of Energy Consumed Per Bit Transmitted. *Nat. Photonics* **2010**, *4*, 648–654.
45. Lindsay, L.; Broido, D, A.; Mingo, N. Flexural Phonons and Thermal Transport in Graphene. *Phys. Rev. B* **2010**, *82*, 115427–115432.
46. Bae, M, H.; Li, Z.; Aksamija, Z.; Martin, P, N.; Xiong, F.; Ong, Z, Y.; Knezevic, I.; Rop, E. Ballistic to Diffusive Crossover of Heat Flow in Graphene Ribbons. *Nat. Commun.* **2013**, *4*, 1734-1–1734-7.
47. Cai, W.; Moore, A, L.; Zhu, Y.; Li, X.; Chen, S.; Shi, L.; Rouff, R, S. Thermal Transport in Suspended and Supported Monolayer Graphene Grown by Chemical Vapor Deposition. *Nano Lett.* **2010**, *10*, 1645–1651.
48. Chen, S.; Moore, A,L.; Cai, W.; Suk, J, W.; An, J.; Mishra, C.; Amos, C.; Magnuson, C, W.; Kang, J.; Shi, L.; Ruoff, R, S. Raman Measurements of Thermal Transport in Suspended Monolayer Graphene of Variable Sizes in Vacuum and Gaseous Environments. *ACS Nano* **2011**, *5*, 321–328.
49. Freitag, M.; Steiner, M.; Martin, Y.; Perebeinos, V.; Chen, Z.; Tsang, J. C.; Avouris, P. Energy Dissipation in Graphene Field-Effect Transistors. *Nano Lett.* **2009**, *9*, 1883–1888.
50. Chen, Z.; Jang, W.; Bao, W.; Lau, C. N.; Dames, C. Thermal Contact Resistance between Graphene and Silicon Dioxide. *Appl. Phys. Lett.* **2009**, *95*, 161910-1–161910-3.
51. Mak, K, F.; Lui, C, H.; Heinz, T, F. Measurement of the Thermal Conductance of the Graphene/ SiO_2 Interface. *Appl. Phys. Lett.* **2010**, *97*, 221904-1–221904-3.
52. Meyer, F. J. C.; Scardaci, V.; Casiraghi, C.; Lazzeri, M.; Mauri, F.; Piscanec, S.; Jiang, D.; Novoselov, K. S.; Roth, S.; Geim, A. K. Raman Spectrum of Graphene and Graphene Layers. *Phys. Rev. Lett.* **2006**, *97*, 187401–187404.
53. Hsu, C. L.; Lin, C. T.; Huang, J. H.; Chu, C. W.; Wei, K. H.; Li, L. J. Layer-by-Layer Graphene/TCNQ Stacked Films as Conducting Anodes for Organic Solar Cells. *ACS Nano* **2012**, *6*, 5031–5039.